LAWRENCE
LIVERMORE
NATIONAL
LABORATORY

LLNL-JRNL-451336

Direct characterization of phase transformations and morphologies in moving reaction zones in Al/Ni nanolaminates using dynamic transmission electron microscopy

J. S. Kim, T. LaGrange, B. W. Reed, R. Knepper, T. P. Weihs, N. D. Browning, G. H. Campbell

August 27, 2010

Acta Materialia

Disclaimer

Direct characterization of phase transformations and morphologies in moving reaction zones in Al/Ni nanolaminates using dynamic transmission electron microscopy

Judy S. Kim [a,b,*], Thomas LaGrange [a], Bryan W. Reed [a], Robert Knepper [c], Timothy P. Weihs [c], Nigel D. Browning [a,b], Geoffrey H. Campbell [a]

a. Condensed Matter & Materials Division, Lawrence Livermore National Laboratory, 7000 East Avenue, Livermore, CA 94550, USA
b. Chemical Engineering & Materials Science / Molecular & Cellular Biology, University of California-Davis, 1 Shields Avenue, Davis, 95616, USA
c. Department of Materials Science & Engineering, Johns Hopkins University, 3400 N. Charles St., Baltimore, MD 21218, USA

* Corresponding author's present address:
Department of Materials, University of Oxford, Parks Road, Oxford, OX1 3PH, UK
Phone: +44 (0)1865 273657, Fax +44 (0)1865 273789

Author's Email addresses:

judy.kim@materials.ox.ac.uk

lagrange2@llnl.gov

reed12@llnl.gov

rkneppe@sandia.gov

weihs@jhu.edu

nbrowning@ucdavis.edu

campbell7@llnl.gov

Abstract:

Phase transformations and transient morphologies are examined as exothermic formation reactions self-propagate across Al/Ni nanolaminate films. The rapid evolution of these phases and sub-μm morphological features require nanoscale temporal and spatial resolution that is not available with traditional *in situ* electron microscopy. This work uses Dynamic transmission electron microscopy (DTEM) to identify intermetallic products and phase morphologies as exothermic formation reactions self-propagate in nanolaminate films grown with 3:2, 2:3, and 1:1 Al/Ni atomic ratios. Single-shot, diffraction patterns with 15 ns temporal resolution reveal that the NiAl intermetallic forms within 10 nanoseconds of the reaction front's arrival in all three types of films and is the only intermetallic phase to form as the reactions self-propagate and quench very rapidly. Concurrently, time resolved imaging reveals a transient cellular morphology in the Al-rich and Ni-rich foils, but not in the equiatomic films. The cellular features in the Al-rich and Ni-rich films are attributed to a cooling trajectory through a two-phase field of *liquid + NiAl*.

Key words: Nickel Aluminides, thin film multilayers, rapid solidification, phase transformations, dynamic transmission electron microscopy

1. Introduction

Reactive nanolaminate films have been studied because of their useful ability to store energy and then release it rapidly. The stored energy can be exploited for various applications requiring localized heating such as soldering temperature-sensitive devices [1-3], igniting other reactions, or neutralizing biological materials [4]. Reactive nanolaminates have also been studied because they enable rapid, self-propagating reactions that present a scientifically interesting case of coupled nonequilibrium processes (atomic diffusion, heat diffusion, chemical reactions, and phase

transformations) that occur over a wide range of length and time scales, and produce unexpected transient structures that relax in microseconds [5].

The self-propagating reactions in nanolaminates are initiated locally by an external stimulus and are characterized by species interdiffusing normal to the layers, heat being released into the film and environment due to this intermixing, and a reaction front propagating parallel to the layers of the reactive multilayer foil (RMLF). The zone of dynamic mixing, which we will refer to as the reaction front, can have extremely high heating rates of ~10^6-10^9 K/s [6]. In addition, reaction front velocity and temperature can be manipulated by tailoring layer thickness, foil chemistry, and the extent of pre-mixing [7-9,1]. However, little is known as to how the reactants mix and transform into the final reaction products. Increasing our knowledge of the transient behavior would provide insights into the nature of rapid formation reactions and could provide improved methods for tailoring reactive laminate performance for specific engineering applications.

The combination of fast reaction velocities and sub-micron features in these self-propagating reactions makes direct analysis of phase transformations, morphological progressions, and rate-limiting mechanisms challenging. Recent studies that utilize high speed imaging or in situ X-ray diffraction of self-propagating reactions in nanolamiantes have increased our understanding of these reactions [6,10,11], but still lack nanoscale temporal and spatial resolutions. The Dynamic TEM (DTEM) was developed [12-14] to address this opportunity in characterization capability by using a photoemitted electron pulse to probe dynamic events with single-pulse, “snap-shot” diffraction and imaging at 15 ns resolution (Figure 1). Using this capability, the moving reaction front of reactive nanolaminates has been observed *in situ* [5] in both real and reciprocal space. DTEM images show a transient cellular morphology that disappears during cooling. Such studies provide an opportunity to gain fundamental insights into the mechanisms that control the self-propagation of exothermic reactions. Here we use Dynamic transmission electron microscopy to identify intermetallic products and phase morphologies as

exothermic formation reactions self-propagate in Al/Ni nanolaminate films of Al-rich, Ni-rich and equiatomic chemistries.

2. Experimental Methods

2.1 Materials studied

The RMLF samples of this work have one of three Al-Ni atomic compositions: Al-rich, Ni-rich, or balanced, with Al to $Ni_{0.91}V_{0.09}$ atomic ratios of 3:2, 2:3, and 1:1, as detailed in Table 1. The layers were magnetron sputtered from an 1100 Al alloy target [99 wt.% Al, 0.87% (Si, Fe), 0.12% Cu] (or 99.999% pure Al in the case of the Ni-rich foils) and a Ni target containing 7 -wt.% (9 at%) V. The vanadium is added to the Ni to reduce its magnetism and thereby ease its sputter deposition. The V substitutes for Ni atoms on the crystalline lattice and continues to be a substitutional alloying element in the intermetallic reaction products observed here.

Table 1
Stoichiometries and initial compositions of reactive foils examined

	Atomic Ratio Al : $Ni_{0.91}V_{0.09}$	Bilayer Length (nm)	No. of Bilayers	Total Thickness (nm)
Al-rich	3:2	21	6	125
Balanced	1:1	21	6	125
Ni-rich	2:3	25	5	125

The films were deposited onto polished NaCl crystals for lift-off onto clamping Cu TEM grids using deionized water. A bilayer is defined as one Al layer and one Ni layer. The films were capped on top and bottom with half-thickness Ni layers to avoid Al oxidation during handling in air as well as during the actual experiment, while still maintaining the desired stoichiometry. The films examined had an as-grown (unreacted) total thickness of 125 nm and 5-6 bilayers, measured by profilometer and TEM cross-section micrographs.

2.2 Experimental Setup

Nanosecond *in situ* electron microscopy is achieved using laser induced photoemitted electrons in

a single, 15 ns long cluster of $1x10^8$ electrons in a dynamic TEM (DTEM) [15]. This short pulse of electrons probes a 15 ns window in the evolution of a TEM specimen and is collected on a high sensitivity *TVIPS TemCam-F224HD* CCD camera, producing a single-shot image or diffraction pattern. This method, previously described in more detail [16-21], is a pump-probe technique with the ability to characterize fast materials processes on the 15 ns time scale and the 10 nm length scale. The single-shot approach is useful for observation of irreversible processes (that cannot be repeatedly "pumped" to invoke a reoccurring event as in "4D electron microscopy"[22], as is the case with RMLFs.

These DTEM experiments used a Nd:YAG pump laser to initiate mixing in the reactive nanolaminates with conditions of 80 μm $1/e^2$ radius spot size on the specimen, 4-15 μJ energy, and 12 ns full-width at half-maximum pulse duration at the sample. Before running experiments, the specimen drive laser settings were optimized to minimize the specimen interaction area to a small, round spot. In addition, pulse energy was adjusted to a level just above the sample-dependent threshold required to initiate a self-propagating reaction in order to avoid extraneous warming of the film. The threshold energies using the pump laser were found to be 4.0 ± 0.1, 6.5 ± 1.5, 12.9 ± 0.5μJ for the Al-rich, Ni-rich and balanced films, respectively. Because the microstepper motors on the final turning lens were quite coarse on the scale of TEM work, the laser spot was positioned in an area of the sample far removed from the observation point to eliminate its direct effect, and this position was kept constant throughout a series of experiments. The part of the reaction front that is examined in each individual DTEM experiment is then changed by varying the time delay between the pump and probe drive laser pulses.

The orientation of the experimental setup inside of the DTEM is shown in the schematic in Fig. 1. First, the 12 ns Nd:YAG pump laser pulse warms a small region of the RMLF, initiating the reaction at a position far enough from the observation area (hundreds of μm) for the reaction front to reach steady-state propagation at the point of observation. The reaction front radiates in all directions from its initiation site in the freestanding RMLF membrane. Next, the probing electron pulse is photoemitted

from the cathode using a frequency-quintupled 211 nm Nd:YLF laser pulse. Timing boxes can vary the time delay between the two lasers from nanoseconds to seconds. The electron pulse interacts with the foil at a location along the microscope optic axis (away from the initiation site) to probe the specimen.

Like other pump-probe experiments, it is essential to define time-zero as a reference point for all time-delayed experiments. In this work (with the exception of the low-magnification images described below), time-zero is defined by the arrival of the reaction front at the center of the viewing area, or at the optic axis of the DTEM column in Fig. 1. Since we are interested in the variation of the reaction front's structure with time, this definition of time-zero is more convenient than the reaction initiation time (which is ~10 μs earlier). Time-zero is experimentally determined during each session through visual observations of the reaction front's position in multiple images. In diffraction, this definition remains intact, however diffraction is collected from a rather large area (up to tens of microns) and a snap-shot at time-zero would include information from regions both before and after the reaction front, just as in the images. The typical time-resolved diffraction experiments in this work are made up of a series ("before," "during," and "after") of RMLF snap-shots. As-deposited and fully reacted diffraction patterns are collected from the foils in a static state and are used as references during experimental setup and for camera length calibration during data analysis.

Diffraction experiments were collected using a 100 μm condenser aperture to remove the electrons that would strike the sample at high angles (thus improving reciprocal-space resolution). Rather than using a selected area diffraction (SAD) aperture, the pulsed beam was spread to a limited diameter of illumination (3.3, 11, 26 μm for the Al-rich, Ni-rich, and balanced foils respectively) and held constant for each given series. This method was essential for collecting enough electrons for single-shot interpretation.

3. Results

3.1 Diffraction

Time-resolved diffraction studies of the reactive foils use a single 15 ns electron pulse to probe the reacting specimen at a specified time after the pump laser initiation. Diffraction ring pattern data are rotationally averaged for a more quantitative display of ring intensity ratios. They are plotted and examined as intensity versus position in reciprocal space. The results in Fig. 2 show that all three stoichiometries show only a single transition to the intermetallic, ordered B2 phase, NiAl. Diffraction snap-shots acquired before the mixing front arrives, clearly show the initial as-fabricated samples as a combination of FCC Al and FCC Ni. The curves acquired as the reaction front arrives (at t = 0 μs) contain peaks corresponding to diffraction rings of B2 NiAl. The diffraction peaks obtained after the reaction zone passes can be entirely attributed to B2 NiAl. Crystalline peaks are consistently present in all diffraction patterns covering many different time delays, indicating that the films remain crystalline, at least in part, throughout the dynamic mixing event.

As the hot reaction front passes the observation area probed by the electron pulse, background intensity increases and the diffraction ring patterns become diffuse due to increased thermal diffuse scattering. Seconds later, after the specimen is fully reacted, the samples have converted completely to NiAl without signs of transitions to other phases such as Al_3Ni_2 or $AlNi_3$, unlike other findings from differential scanning calorimetry and x-ray diffraction work of various material systems of nanolaminates [6,23,24]. The result that all three types of these far-from-equilibrium nanolaminates make a single transition to the NiAl phase should be noted since the material systems should form various other intermetallic phases [25] for the 3:2 and 2:3 Al:Ni compositions, when in equilibrium.

We observed occasional timing inconsistencies indicating that the reaction initiation may have varying incubation times or propagation speeds. A few experiments showed that the reaction front did not arrive according to calculations with errors as large as 0.3 μs, but when observed afterwards, the RMLF indeed did react. If the reaction front was traveling 13 m/s, the 0.3 μs time differential implies

that the reaction front was lagging behind predicted values by at least 3.9 μm. With the timing jitter of the sample drive and cathode drive lasers being only ± 1 ns, the 0.3 μs (3.9 μm) delays cannot be attributed to experimental controls. This variability of timing is interesting for engineering applications and should be explored further in future work.

Thermal diffuse scattering (TDS) effects increase the background, blur the ring patterns and reduce the intensity of higher order reflections for up to 20.4 μs in the Al-rich diffraction curve. Data at longer time delays were not acquired since the reacted foils would often tear and move far out of the optimum electron probing volume of the objective lens. By directly comparing 20.4 μs and "after" data (effectively collected when the thin foil is cooled to ambient temperature), which are both single-shot acquisitions, the TDS effects are apparent by the blurring of peak details. Snap-shot data collected after the mixing event shows sharper peaks and less TDS. This long-lasting TDS effect is also found in the atomically balanced and Ni-rich foils.

3.2 Imaging

To observe the layer mixing process and the progression of the reaction front morphology, the dynamic reaction front was directly imaged using single pulses. Fig. 3, a series of low magnification images with a ~(500 μm)^2 field of view, shows how the reaction propagates radially from the laser initiation site. The mixing front appears in the "during" micrograph as a sharp change in contrast that has traveled a particular distance following reaction ignition and prior to the snapshot image. Again, the time delay is the difference between the ignition and the snapshot image. In this low-resolution view, the reaction front appears moderately smooth and featureless for the three types of samples studied. After the reaction front passed, the individual layers have mixed and the intermetallic NiAl has nucleated as confirmed by the diffraction results of Fig. 2.

3.2.1 Al-rich nanolaminates

In search of morphological details at the reaction front at higher resolution, we begin with the Al-rich system, grown with Al : $Ni_{0.91}V_{0.09}$ at a 3:2 atomic ratio. In bright field imaging conditions, the reaction front is closely followed by an elongated, finger-like cellular structure, defining the start of the cellular front (Fig. 4). Although the features are somewhat blurred at this front, they appear to have slightly scalloped edges. In this bright field image (Fig. 4), the transient cellular features are observed in their entirety, from start to finish, and are measured to be ~3.2 μm long with a periodicity of 390 ± 55 nm. Based on the length of the cellular features and the reaction front velocity, one can deduce that a given point on the foil remains in a cellular morphology for roughly 230 ns.

Immediately behind the reaction front, the material was found to be nanocrystalline NiAl, confirmed by diffraction. The electron pulse interaction area was limited to a 3.3 μm diameter region on the foil, making the Al-rich diffraction work accurate only to this dimension. As the metastable cellular features are quite short, there is a small possibility that other intermetallic phases may be forming temporarily in this cellular region. This, however, is unlikely, because in over 20 Al-rich diffraction experiments near the reaction front (t=0 sec) we only observed conversion to the NiAl phase, or on rare occasions, the complete lack of a phase change due to the reaction initiation incubation error discussed earlier. No intermetallic phases aside from NiAl were detected at any point in time. Thus if there are other crystalline phases present, they must exist either very briefly or in very small quantities, or both.

Finally at longer times, the NiAl coarsens to large intermetallic grains that often traverse the entire 125 nm thickness of the foil found by post mortem cross-sectional TEM and energy-dispersive x-ray spectroscopy (EDS).

3.2.2. Ni-rich nanolaminates

The Ni-rich system has been studied previously [5] in the same manner. Similar bright field results are shown (Fig. 5) for comparative analysis to the Al-rich system described above. The cellular

features are notably longer than those found in Al-rich films, having a length greater than 40 μm (equivalent to a 3 μs duration at a given point) and a periodicity of 790 ± 220 nm in width. The Ni-rich cellular features have a longer and a more uniform morphology compared to the markedly tortuous features found in the Al-rich foils (Table 2). However, in a similar manner they show a distinct line of formation and gradual termination, establishing a transient nature. The dark lines between the cellular features are 220 ± 80 nm wide.

Table 2
Comparison of quantified cellular feature measurements of Figures 4 and 5

	Periodicity	Length
Ni-rich (2 Al : 3 Ni)	790 ± 220 nm	> 40 μm [a]
Al-rich (3 Al : 2 Ni)	390 ± 55 nm	3.2 ± 0.3 μm

[a] The length of the features indicated are greater than 40 μm, however restrictions on the image field of view limited a more accurate measurement. Lower magnifications would increase the field of view, but at such lens settings, the data would not produce a true bright field image.

Like the Al-rich films, it appears that the cellular features behind the reaction front are at least partially solid NiAl intermetallic. Diffraction data obtained for these Ni-rich foils (Figure 2) confirmed the almost immediate formation of NiAl at the reaction front with an error in timing of ± 0.3 μs. In diffraction work shown earlier, a condenser aperture was used so that the beam interacts with a round sample area 11.2 μm in diameter, making the obtained phase information accurate to this dimension, far smaller than the 40 μm width of the cellular formation region. Diffraction work of the previous section taken in synchronization with the arrival of the visible reaction front (from imaging) proves that crystalline NiAl intermetallic formation occurred within 300 ns of t = 0, which would be equivalent to a distance 3.9 μm behind the reaction front. Since crystalline NiAl formed less than 3.9 μm behind the reaction front, and the cellular features are present at this position, the cellular structures must contain crystalline NiAl.

The dark intensity between the “cells” fades away in the last micrograph of the series in Fig. 5, at a point in time where the reaction should have completed some microseconds earlier. The solid

solubility range of the NiAl B2 phase increases as the temperature drops [25], so that at room temperature nearly all of the excess nickel could be re-absorbed into a stable homogeneous B2 structure with a Ni:Al ratio near 3:2. Post-mortem EDS examination (Table 3) indicates that this occurs and is discussed in a following section.

To understand how quickly the cellular front or boundary forms, we consider that the motion blur of the features in the time-resolved micrographs is limited to ~ 200 nm based on the 15 ns temporal resolution and reaction front velocity of 13 m/s. From the time-resolved images, the sharp onset of the cellular microstructure begins with only a small 100 nm (equivalent 8 ns) blur in front. This is less than the calculated motion blurring, and it implies that the cellular morphology takes shape at least as fast as the temporal resolution of the DTEM instrument in this configuration (~15ns).

3.2.3. Balanced composition nanolaminates

Fig. 6 shows the results of two series of experiments where the reaction front is observed after it is initiated far outside of the micrograph view and travels from the top left to the lower right. Series A examines a clean RMLF for the observation of the reaction front. The front still appears as a moderately straight, featureless variation in intensity over a distance less than 1 μm wide. (Note that in series A, a slightly condensed disk of illumination was used rather than the completely spread, parallel illumination common to conventional TEM. This was employed simply to maximize the utilization of all electrons passing through the condenser aperture.)

In series B of Fig. 6, the initial foil is contaminated with NaCl crystals that originated from the NaCl substrate. The NaCl is located on the surfaces of the RMLF. As the reaction front passes through the view of the micrograph, the front is not visible as a change in intensity (because of the lack of contrast), but rather, by the lack of NaCl contamination. Just behind the reaction front, the foil appears to be free of surface debris. A likely explanation is that, since the reaction front region is quite hot, the

weak bonds are broken between the RMLFs and the NaCl, releasing NaCl into the vacuum of the DTEM. After the foil is completely reacted, grains have grown, and salt crystals are not present. In both experiments of Fig. 6 the cellular structures are not observed.

Similarly, as in all stoichiometries examined, the B2 NiAl intermetallic that formed behind the reaction front coarsened into much larger grains (~250 nm in diameter) as shown in the "after" experiment frames. These large grains are typically observed in post-mortem examination indicating that a high density of small grains nucleated, then coarsened into a lower density of large grains. Although the balanced foils might be expected to coarsen into larger grains than in the Ni or Al-rich foils as they dwell at high temperatures for longer times, it appears that the 125 nm film thickness limits the extent of the grain growth similarly in all experiments.

3.3. EDS analysis

The compositions of the RMLF samples were measured by EDS analysis, where several spectra were averaged from acquisitions of ~60 seconds live time and 40% ± 4% dead time. Compositions of the unreacted and reacted states are compared for Ni-rich and Al-rich foils (Table 3). Vanadium preferentially substitutes for Ni in the ternary intermetallic phase NiAl-V, confirmed by thermal conductivity measurements [26]. The EDS data shows very little change in V content after the reactions propagate across the samples. Thus far, there is no evidence that V segregates at any point during the process, or that it alters the reaction dynamics.

Table 3
TEM-mode EDS analysis of unreacted and reacted foils for average composition changes

		Al at%		Ni at%		V at%		O at%	
Ni-rich (2 Al : 3 Ni)	Unreacted	37.9	± 1.5	56.9	± 1.2	5.3	± 0.5	--	--
	Reacted	38.1	± 5.6	57.4	± 4.9	4.5	± 0.8	--	--
Al-rich (3 Al : 2 Ni)	Unreacted	56.7	± 2.3	40.2	± 2.2	3.1	± 0.1	0.0	--
	Reacted	49.0	± 1.9	44.0	± 3.5	3.9	± 0.6	3.2	± 2.3

Ni-rich foils did not show a notable change in composition after the foil underwent the mixing reaction. However, Al-rich foils showed a substantial change in the Al:Ni atomic ratio after the mixing reaction completed. The amount of Al decreased 8 at% in the reacted foils and is attributed to the evaporation or sublimation of Al from the samples. Although it was not examined extensively, position dependent x-ray spectra were collected from Al-rich foils with respect to the laser initiation site. The Al percentage gradually decreased with closer proximity to the laser initiation site over a range of several hundred microns. This correlated decrease was small and is reflected in the error of Table 3. Additionally, the Al-rich samples exhibit the introduction of 3 at% oxygen, signifying that a small amount of aluminum oxide formation occurs.

There are two main possibilities for the introduction of oxygen: oxidation with molten Al may occur during the reaction propagation or it may transpire long after the reaction passes, as the sample is removed from the microscope vacuum and introduced to the atmosphere. It is possible that oxygen in the form of H_2O would be available for bonding to the specimen inside the vacuum of the column as the vacuum near the sample is estimated to be approximately10^{-4} Pa. It is also possible that the excess Al at surfaces and grain boundaries becomes oxidized after the dynamic experiments as specimens are left in atmosphere.

4. Discussion

Al/Ni reactive multilayer films are deposited in a state that is far from equilibrium. However, as the films react, the combination of high reaction temperatures and nanoscale diffusion distances allow them to approach equilibrium rapidly. Thus, to help understand the presence of morphological transients in the Al-rich and Ni-rich samples and the lack of such transients in the balanced samples we consider regions of the equilibrium Al-Ni phase diagram where phase separation of the NiAl intermetallic and Al-Ni liquid are expected. Although the samples may not achieve full equilibrium at

high temperatures and even though small V contributions are not considered, the simple Al-Ni equilibrium system serves as an unyielding point of reference for the transient states of these reactive nanolaminates

Considering the reaction temperature (~1700 ± 100 K calculated by thermal expansion in diffraction [5]) and as-grown chemical compositions, the Ni-rich and Al-rich foils both fall into two-phase fields of NiAl + liquid on either side of the congruent melting point in the equilibrium phase diagram [25]. The stoichiometrically balanced foils are confined to the solid NiAl region of the phase diagram throughout the reaction process and fall short of entering the liquid phase field. Thus, the equilibrium phase diagram suggests the Al-rch and Ni-rich samples could show phase separation while the balanced foils should not.

The reaction front regions of all foils are observed to be at least partially solid at all times by crystalline diffraction patterns. This is within the time resolution of 15 ns, equivalent to a maximum of 200 nm of reaction front travel. In addition, time-resolved image data suggest that cellular features form in a short time of < 100 ns. This leaves only two types of phenomena that can explain the sudden formation of the cellular structure: *solid + liquid* or *solid + solid* phase separations.

Observations of cellular-type structures in other materials systems are known to occur in dendritic solidification, cellular precipitation, and eutectoid transformations (pearlite formation) and the dimensions of the structures often vary inversely with growth rate [27-29]. Here, in terms of dimensions, the plan view images in Figs. 4 and 5 suggest the periodicity of cellular features extends across the thickness of the multilayer structure. In addition, they show that the transient structures have in-plane dimensions (390 ± 55 nm and 790 ± 220 nm periodicity) that greatly exceed the bilayer thickness of the RMLF (21-25 nm).

The idea that the phase separation is governed by a mechanism of purely solid state diffusion [30] is improbable considering that features 390 to 790 nm wide form in ~100 ns. Intrinsic solid state

diffusivity or diffusion coefficients, D, are 1.9 and 0.65 $\mu m^2/s$ at T_m and D_0, the pre-exponential factor (which is independent of pressure and temperature) is 1.7 and 1.9 m^2/s for Al and Ni respectively [31]. Even at elevated temperatures, the diffusivities are too low to account for the features observed with these large separation distances. Using the numbers above we calculate a characteristic distance for solid state diffusion, $d=(Dt)^{1/2}$, of approximately 0.3 nm. If we use the calculated diffusivity of Ni in *liquid* Al of 1.8×10^{-8} m^2/s [32] at 1770 K, then the characteristic length is about 40 nm, nearly twice the foil bilayer thickness, therefore enough to ensure complete mixing of neighboring layers but not enough to explain formation of the cellular structure (390 to 790 nm) via liquid state diffusion in ~100 ns. Thus the explanation must invoke a mass transport mechanism significantly faster than solid or liquid state atomic diffusion, leaving bulk convective motion in the liquid phase as the most likely candidate.

Liquid is capable of very rapid convective motion once it forms as a separate phase, including beading up on a surface under the influence of surface tension. This is especially true on small size scales, since the surface energy driving the motion scales quadratically with size while the mass scales cubically. Therefore we hypothesize that the observed cellular structures arise from a complex evolution of mechanisms, as follows: When the heat from the reaction front arrives at a given point, solid-state atomic diffusion is initiated at some unknown time before the cellular front, with Ni being the more rapidly diffusing species. The atomic mixing releases heat and further accelerates the process. When the local temperature is high enough, the Al layers melt and atomic intermixing near the Ni layers accelerates even further. At this stage the liquid Al(Ni) layers are most likely still aligned parallel to the thinning Ni layers. The liquid layers provide enhanced mobility through convective flow and could permit rapid coalescence of the liquid layers into thicker volumes that minimize interface energies. If the newly formed liquid volumes extend through the thickness of the films, they would be visible as cellular structures in plan view, as seen in Fig. 4 and 5, and one would expect them to form convex curvature at the surface-vacuum interfaces to minimize surface energies. As the liquid Al(Ni) layers are

coalescing, atomic diffusion in the liquid (near the interfaces) can lead to chemical ordering and then to the nucleation of NiAl and the displacement of excess elements. Thus, we hypothesize that the cellular structures form in the Al-rich and Ni-rich samples through a coalescence of the liquid layers within the films and the nucleation of the B2 NiAl intermetallic. When these samples cool and re-enter a single-phase region, the remaining liquid is absorbed back into the solid B2 NiAl intermetallic.

This hypothesis is consistent with the observations reported here and with the known thermodynamic properties of the materials. It is especially telling that the balanced 1:1 stoichiometric foils do not produce a visible transient cellular structure during reaction propagation. At 1700 K, they are expected to transition directly into NiAl, as is detected in the diffraction patterns. The calculated maximum temperature does not exceed the NiAl melting temperature of 1911 K. Thus, while the Al layers near the reaction front will melt and thereby enhance chemical mixing, the liquid phase is not an equilibrium phase during the rapid heating experiment. Only the B2 NiAl intermetallic is in equilibrium in the binary samples. Thus, the binary samples are unable to form liquid solutions that are stable enough to allow for coalescence and formation of a solid/liquid cellular structure. The lack of cellular structure in the stoichiometric film therefore supports the hypothesis that bulk motion of the liquid is essential to the formation of these structures.

Unlike slow-heating experiments [23], our observations of the off-stoichiometric foils show that the B2 NiAl phase is the first and only intermetallic phase to nucleate and grow near the hot reaction front. This is consistent with the hypothesized *solid + liquid* mechanism in which NiAl is formed shortly after the thermal front passes. We estimate the thermal front to reach 3.7 μm ahead of the visible cellular front based on the assumption of a linear thermal profile (see Appendix). Within this region, it is likely that atomic mixing and partial layer melting occur before any intermetallic forms because the B2 NiAl should form when the local chemistry is nearly balanced. This would require significant Ni diffusion and the subsequent heat release and melting of the Al layers. Because of experimental limitations

involving thermal diffuse scattering and low signal-to-noise ratios, the DTEM diffraction measurements are unable to detect any minority liquid constituent that may be present before the cellular front. However, in situ XRD studies of similar Al/Ni nanolaminates have detected Al(Ni) liquids during the self-propagating reactions [6].

Further in support of a transient liquid phase, several different analytical studies (HAADF STEM, XEDS, and EELS) have shown that there is an increase in foil thickness at the narrow dark regions between the "cells" [5]. Such increases in thickness can be attributed to the liquid regions beading up at the sample surface during the dual phase transient state and then persisting on cooling from a solid-liquid mixed region into a single-phase solid region of the phase diagram. The presence of liquid can also explain the observed contrast of the cellular features as the liquid phase, which increases thermal diffuse scattering, produces darker image intensity. Some of the dark intensity can also be attributed to the liquid beading up in lines on the surface and the resulting mass thickness contrast.

The hypothesized liquid-solid mechanism also offers a potential explanation of the X-ray EDS studies in which a comparison of pre- and post-mortem Al-rich foils revealed an obvious change in composition. The Al-rich reacted specimens had lost a significant atomic percentage of aluminum and gained a small percentage of oxygen atoms. If Al-rich liquid is exposed on the surface at temperatures well above aluminum's normal melting point, this would allow the surface atoms to evaporate rapidly into the vacuum of the microscope column. During this time (estimated at 230 ns from the length of the cellular features), Al atoms would also have an opportunity to oxidize with H_2O contamination in the column, thus accounting for the increase in post-mortem oxygen content.

Whatever the mechanism of Al depletion in the rapid reactions of the Al-rich foils, it should affect the transient morphology as the composition gradually (within hundreds of nanoseconds) moves closer to 1:1, complicating the trajectory through the two-phase field. The Al depletion clarifies why the final phase is NiAl despite the growth composition that could lead to Al_3Ni_2 in a second, late forming

phase transition, as observed by time-resolved diffraction [6] in thicker foils that have less opportunity for the Al to vaporize.

The oxidation reaction was unexpected because RMLFs were grown to terminate with half-thickness Ni layers (3.2 nm and 6.2 nm in the Ni-rich and Al-rich samples respectively), specifically to reduce the chance of an oxidation reaction. The evident oxide formation complicates the reaction thermodynamics as it is another exothermic reaction contributing to the dynamics. However, the timing of the oxidation reaction is crucial relative to the main mixing reaction in understanding its influence on the overall reaction temperature and phase formation that would require further study to elucidate.

The length of the cellular features may be related to time scales associated with atomic mobility. Al-rich foils are expected to have shorter such time scales than the Ni-rich foils for four reasons: (1) more Al atoms are present, and Al has a lower melting point and greater mobility at a given temperature than Ni, thus more of the liquid phase should form, accelerating (as argued above) the mass transport, (2) the Al-rich foils were grown with a shorter bilayer distance of 21 nm vs. 25 nm, so that even with the same mobility the atoms had less distance to travel in the Al-rich film to complete the mixing event, (3) the liquid phase striations are more closely spaced in the Al-rich foils, so again the time scale for evolution of these structures would be expected to be reduced, and most prominent, (4) the evaporation of Al significantly lowers the foil temperature and changes the composition, enhancing solidification rates and driving the system into the single phase NiAl region. Due to the high heat of vaporization of Al (283 kJ mol^{-1}), evaporating 8 at% Al can cool the foil by as much as 800 K (assuming an initial temperature of 1700 K). Although this estimate is an upper bound, it indicates that concomitant effects of Al depletion and evaporative cooling lead to more rapid solidification of NiAl phase, which together with above mentioned effects, may account for the shorter cellular features indicative of faster evolution.

The differences in the periodicity of the cellular structures between the Al-rich and Ni-rich foils could be due to several effects, including the reaction driving force, grain size, and layer morphology and thickness. Identifying the origin of the observed difference in periodicity would require further investigation to probe the influences of these various effects.

Taken together, these findings reveal unexpected complexity in the dynamics, including phenomena such as spontaneous structure formation on a sub-micron scale, the important role of the liquid phase in the reaction propagation, and possible effects of rapid evaporation and oxidation that further alter the dynamics. Moreover, these effects appear to be markedly different in varied stoichiometries, especially in the 1:1 stoichiometry in which most of the effects do not appear at all. These types of measurements can give insight into how processes on different time and length scales contribute to the complex unfolding of material events far from equilibrium.

5. Conclusion

In all three types of RMLFs studied, the NiAl intermetallic formed within nanoseconds after the mixing reaction front and it is the only phase present after the foils are reacted. Dynamic imaging revealed the presence of transient cellular structures only in off-stoichiometric foils. The cellular features are found to form as the material passes through a two-phase field of liquid + NiAl. Varying dimensions of the cellular features appear, which we speculate can be traced to differences in excess reaction energy and atomic mobility. Unlike in slow heating experiments, Al_3Ni_2 does not form in Al-rich foils due to Al depletion during the self-propagating reactions; therefore, the material at the reaction zone does not travel through a purely thermal trajectory into the two-phase field of liquid + NiAl. Finally, this study confirms that new questions on very fine spatiotemporal scales can be answered using dynamic TEM.

6. Acknowledgements

We thank Prof. O. Knio for useful discussions. We thank Phil Ramsey and Troy Barbee Jr. for making the Ni-rich RMLF. Much of this work performed while JSK was at University of California, Davis and supported by the Lawrence Scholar program at Lawrence Livermore National Laboratory. TL, BWR, NDB, and GHC supported by the US Department of Energy, Office of Science, Office of Basic Energy Sciences, Division of Materials Science and Engineering. RK and TPW supported by Lawrence Livermore National Laboratory through grant number B562528 and by the Office of Naval Research through grant number N00014-07-1-0740. This work performed under the auspices of the US DOE by LLNL under contract DE-AC52-07NA27344.

7. Appendix

If one assumes a constant and linear thermal profile moving at a velocity, v, one can calculate the distance, Δx, over which the temperature rises from 300 K to a maximum of 1800 K. One can simply use the heat released by the foil as the reaction propagates a distance Δx or one can use the heat needed to raise the Ni/Al foil to 1800 K over the distance Δx. Both are shown below for a velocity of 13 m/s. Note that the width of the thermal ramp is only ~3.7 μm.

$$\frac{dQ}{dt} = K\frac{dT}{dx}$$ where K is thermal conductivity and dQ has units of J/m^2

$$\frac{\Delta Q}{\Delta t} = K\frac{\Delta T}{\Delta x}$$

$$\Delta x = K\frac{\Delta T \Delta t}{\Delta Q}$$ where ΔQ has units of J/m^2

$$\Delta x = K\frac{\Delta T\frac{\Delta x}{v}}{\Delta H_{rx}\rho\Delta x}$$ where ΔH_{rx} has units of J/g and v is velocity

$$\Delta x = \frac{K\Delta T}{\Delta H_{rx}\rho v}$$ where K is volume averaged and ρ is mass weighted

$$\Delta x = \frac{(161.2W \cdot m^{-1}K^{-1})(1500K)}{(1000J/g)(5.1\times10^{6}g/m^{3})(13m/s)} = 3.7\mu m$$

References

[1] Wang J, Besnoin E, Duckham A, Spey SJ, Reiss ME, Knio OM, Weihs TP. Journal of applied physics 2004;95:248-256.

[2] Barbee J, Weihs TP. Method for Fabricating an Ignitable Heterogeneous Stratified Metal Structure. U.S. Patent Patent No. 5547715, 1996.

[3] Wang J, Besnoin E, Duckham A, Spey SJ, Reiss ME, Knio OM, Powers M, Whitener M, Weihs TP. Applied physics letters 2003;83:3987-3989.

[4] Zhao SJ, Germann TC, Strachan A. Journal of chemical physics 2006;125:164707.

[5] Kim JS, LaGrange T, Reed BW, Taheri ML, Armstrong MR, King WE, Browning ND, Campbell GH. Science 2008;321:1472-1475.

[6] Trenkle JC, Koerner LJ, Tate MW, Gruner SM, Weihs TP, Hufnagel TC. Applied physics letters 2008;93:081903.

[7] Floro JA. J. vac. sci. technol. a 1986;4:631-636.

[8] Ma E, Thompson CV, Clevenger LA, Tu KN. Applied physics letters 1990;57:1262-1264.

[9] Mann AB, Gavens AJ, Reiss ME, VanHeerden D, Bao G, Weihs TP. Journal of applied physics 1997;82:1178-1188.

[10] Adams DP, Rodriguez MA, McDonald JP, Bai MM, Jones E, Brewer L, Moore JJ. J. appl. phys. 2009;106:093505.

[11] McDonald JP, Hodges VC, Jones ED, Adams DP. Appl. phys. lett. 2009;94:034102.

[12] LaGrange T, Armstrong MR, Boyden K, Brown CG, Campbell GH, Colvin JD, DeHope WJ, Frank AM, Gibson DJ, Hartemann FV, Kim JS, King WE, Pyke BJ, Reed BW, Shirk MD, Shuttlesworth RM, Stuart BC, Torralva BR, Browning ND. Applied physics letters 2006;89:044105-3.

[13] LaGrange T, Campbell GH, Colvin JD, Reed B, King WE. Journal of materials science 2006;41:4440-4444.

[14] Taheri ML, Lagrange T, Reed BW, Armstrong MR, Campbell GH, DeHope WJ, Kim JS, King WE, Masiel DJ, Browning ND. Microscopy research and technique 2009;72:122-130.

[15] Reed BW, LaGrange T, Shuttlesworth RM, Gibson DJ, Campbell GH, Browning ND. Rev. sci. instrum. 2010;81:053706.

[16] King WE, Campbell GH, Frank A, Reed B, Schmerge JF, Siwick BJ, Stuart BC, Weber PM. Journal of applied physics 2005;97:111101-27.

[17] Armstrong MR, Boyden K, Browning ND, Campbell GH, Colvin JD, DeHope WJ, Frank AM, Gibson DJ, Hartemann F, Kim JS, King WE, LaGrange TB, Pyke BJ, Reed BW, Shuttlesworth RM, Stuart BC, Torralva BR. Ultramicroscopy 2007;107:356-367.

[18] LaGrange T, Campbell GH, Turchi PEA, King WE. Acta materialia 2007;55:5211-5224.

[19] LaGrange T, Campbell GH, Reed B, Taheri M, Pesavento JB, Kim JS, Browning ND. Ultramicroscopy 2008;108:1441-1449.

[20] Reed B, Armstrong M, Browning N, Campbell G, Evans J, LaGrange T, Masiel D. Microscopy and microanalysis 2009;15:272-281.

[21] Campbell GH, LaGrange T, Kim JS, Reed BW, Browning ND. J electron microsc (tokyo) 2010:dfq032.

[22] Zewail AH. Science 2010;328:187-193.

[23] Blobaum KJ, Van Heerden D, Gavens AJ, Weihs TP. Acta materialia 2003;51:3871-3884.

[24] Edelstein AS, Everett RK, Richardson GY, Qadri SB, Altman EI, Foley JC, Perepezko JH. Journal of applied physics 1994;76:7850-7859.

[25] Singleton MF. Al-ni. In: Massalski TB, editor. Binary Alloy Phase Diagrams, vol. 2nd. Metals Park, OH: ASM International, 1990. pp. 181-184.

[26] Terada Y, Ohkubo K, Mohri T, Suzuki T. Materials science and engineering a 2002;329-331:468-473.

[27] Sundquist B. Acta metallurgica 1968;16:1413-&.

[28] Langer JS. Reviews of modern physics 1980;52:1-28.

[29] Boettinger WJ, Warren JA. Journal of crystal growth 1999;200:583-591.

[30] Wei H. Acta materialia 2004;52:2645-2651.

[31] Brown AM, Ashby MF. Acta metallurgica 1980;28:1085-1101.

[32] Du Y, Chang YA, Huang B, Gong W, Jin Z, Xu H, Yuan Z, Liu Y, He Y, Xie F-. Materials science and engineering a 2003;363:140-151.

[33] Porter DA, Edington JW. Proceedings of the royal society of london. series a, mathematical and physical sciences (1934-1990) 1978;358:335-350.

Figure captions

Fig. 1. Schematic representation of a DTEM snap-shot process
In a time-zero snap-shot the electron pulse probes the sample as the reaction front passes the center of the microscope optic axis and micrograph (or area used for diffraction). Plan-view observations are made so that the electron pulse transmits through all of the sample layers and the viewing z-direction is normal to the multilayers.

Fig. 2. Rotationally averaged diffraction ring intensities
Snap-shot ring diffraction patterns are displayed as the rotational average with respect to reciprocal spacing for clarity. A, B, and N correspond to foils of Al-rich (3 Al : 2 Ni atomically), balanced (1 Al : 1 Ni at.), and Ni-rich (2 Al : 3 Ni at.) respectively. Timing of the single-shot data acquisition is as indicated with reference to the mixing reaction front arrival at the viewing optic axis, t_0 (see Fig. 1).

Fig. 3. Series of low magnification single-pulse images of the nanolaminates
The foils are shown at times before (left), during (center), and after (right) the propagation of the mixing reaction. The center micrographs show the partially mixed state of the reactive foils at the following times after sample drive laser initiation: 8.0 μs in Al-rich (A), 13.2 μs in balanced (B), and 9.9 μs in Ni-rich (C) foils. The fully reacted foils are a NiAl intermetallic phase, occasionally displaying tearing and rumpling of the electron transparent material (A, right).

Fig. 4. Time resolved image of the reaction front in Al-rich foils
Foils grown to a 3:2 Al:Ni ratio imaged with 15 ns temporal resolution. The dotted line approximately indicates the mixing front as it travels towards the lower left of the image. Cellular features are only 3 μm long. This micrograph was generated using a 50 μm objective aperture.

Fig. 5. Plan-view bright field micrographs of the Ni-rich foils
This series of images shows the progression of the Ni-rich mixing front as it enters the image view (A), after 970 ns the structure moves further from the initiation point (B), and begins to fade away after the Al/Ni layers have completed mixing (2.3 μs) (C).

Fig. 6. Dynamic series of the reaction front progression in stoichiometrically balanced foils
The two series of single-pulse images show the passing of the reaction front in the center *during* frames at (A series) 18 μs and (B series) 7.3 μs. The B series has many ~1 μm features of residual NaCl substrate crystals that disappear as the reaction front passes.

Direct characterization of phase transformations and morphologies in moving reaction zones in Al/Ni nanolaminates using dynamic transmission electron microscopy

Judy S. Kim [a,b,*], Thomas LaGrange [a], Bryan W. Reed [a], Robert Knepper [c], Timothy P. Weihs [c], Nigel D. Browning [a,b], Geoffrey H. Campbell [a]

Figures:

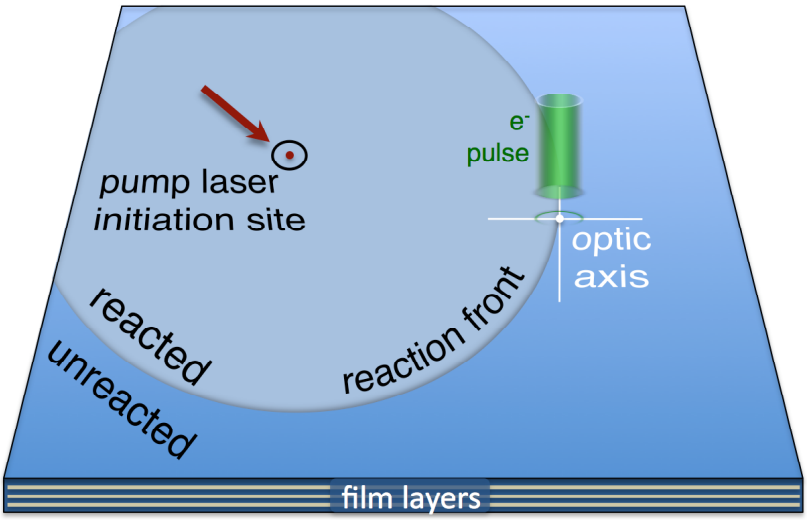

Fig. 1. Schematic representation of a DTEM snap-shot process
In a time-zero snap-shot the electron pulse probes the sample as the reaction front passes the center of the microscope optic axis and micrograph (or area used for diffraction). Plan-view observations are made so that the electron pulse transmits through all of the sample layers and the viewing z-direction is normal to the multilayers.

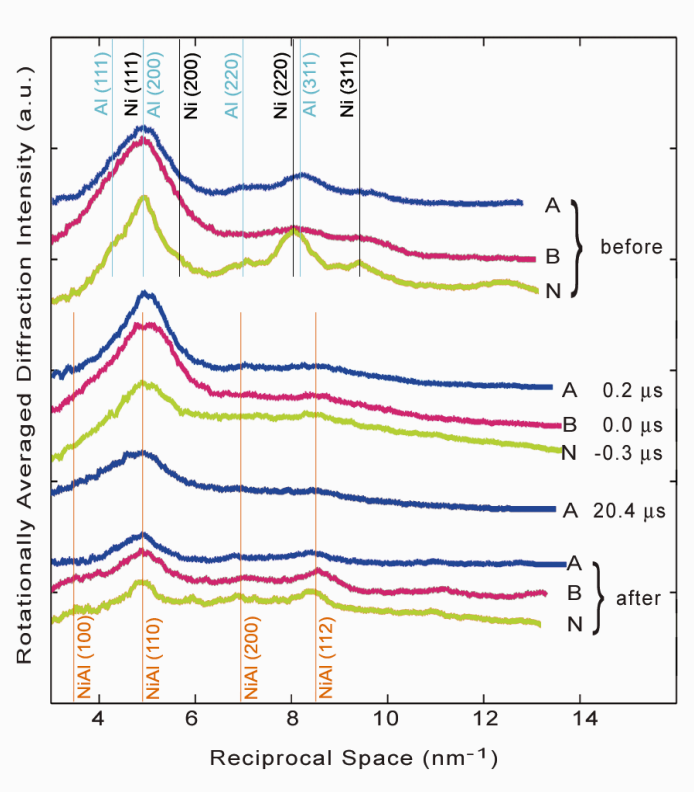

Fig. 2. Rotationally averaged diffraction ring intensities

Snap-shot ring diffraction patterns are displayed as the rotational average with respect to reciprocal spacing for clarity. A, B, and N correspond to foils of Al-rich (3 Al : 2 Ni atomically), balanced (1 Al : 1 Ni at.), and Ni-rich (2 Al : 3 Ni at.) respectively. Timing of the single-shot data acquisition is as indicated with reference to the mixing reaction front arrival at the viewing optic axis, t_0 (see Fig. 1).

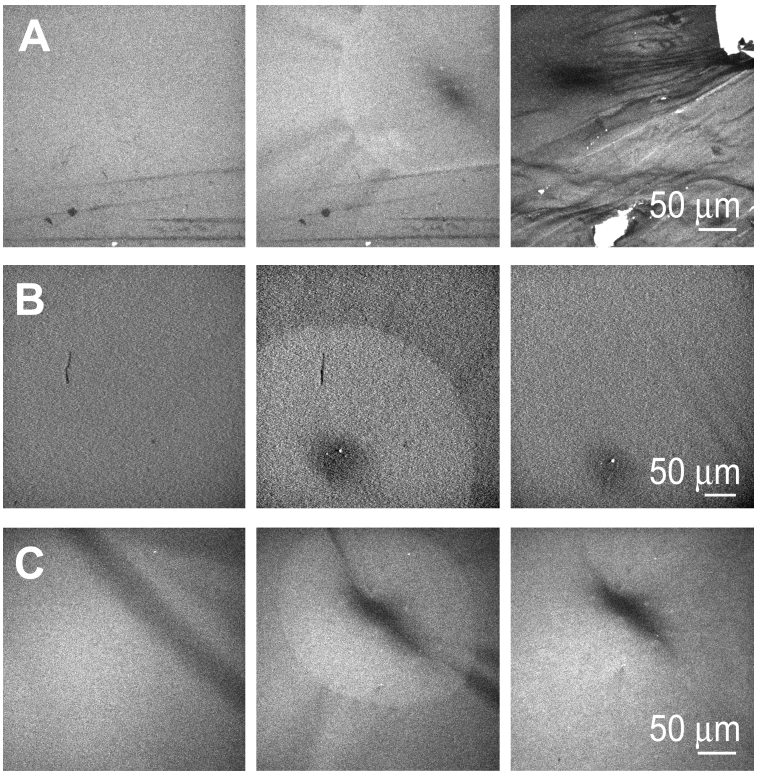

Fig. 3. Series of low magnification single-pulse images of the nanolaminates
The foils are shown at times before (left), during (center), and after (right) the propagation of the mixing reaction. The center micrographs show the partially mixed state of the reactive foils at the following times after sample drive laser initiation: 8.0 μs in Al-rich (A), 13.2 μs in balanced (B), and 9.9 μs in Ni-rich (C) foils. The fully reacted foils are a NiAl intermetallic phase, occasionally displaying tearing and rumpling of the electron transparent material (A, right).

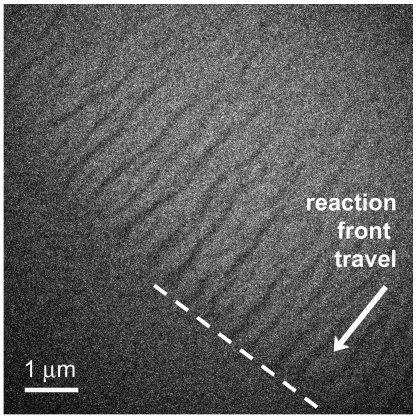

Fig. 4. Time resolved image of the reaction front in Al-rich foils
Foils grown to a 3:2 Al:Ni ratio imaged with 15 ns temporal resolution. The dotted line approximately indicates the mixing front as it travels towards the lower left of the image. Cellular features are only 3 μm long. This micrograph was generated using a 50 μm objective aperture.

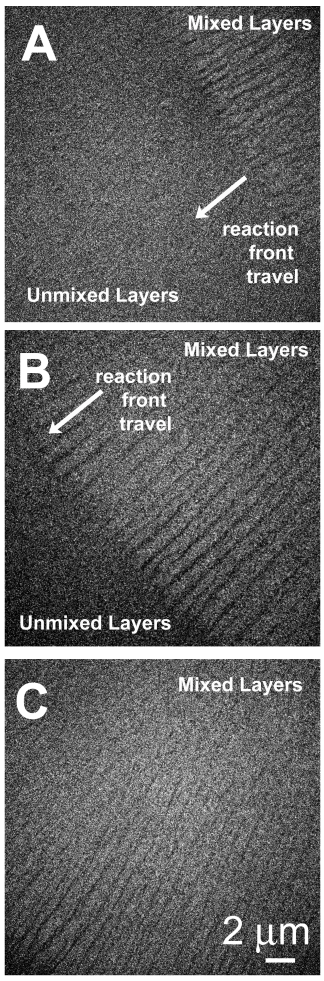

Fig. 5. Plan-view bright field micrographs of the Ni-rich foils
This series of images shows the progression of the Ni-rich mixing front as it enters the image view (A), after 970 ns the structure moves further from the initiation point (B), and begins to fade away after the Al/Ni layers have completed mixing (2.3 μs) (C).

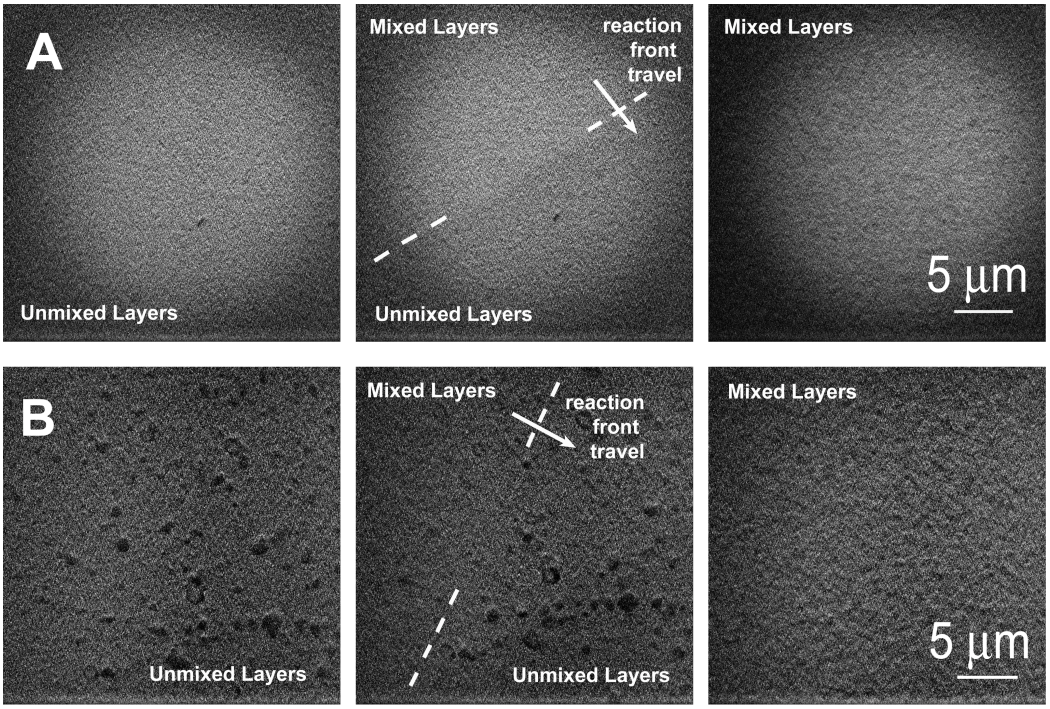

Fig. 6. Dynamic series of the reaction front progression in stoichiometrically balanced foils
The two series of single-pulse images show the passing of the reaction front in the center *during* frames at (A series) 18 μs and (B series) 7.3 μs. The B series has many ~1 μm features of residual NaCl substrate crystals that disappear as the reaction front passes.